

Nonlinear anomalous Hall effect in a collinear antiferromagnetic Weyl metal

Ding-Fu Shao,^{1,*} Shu-Hui Zhang,^{2,*} Gautam Gurung,¹ Wen Yang,³ and Evgeny Y. Tsymbal^{1,§}

¹ Department of Physics and Astronomy & Nebraska Center for Materials and Nanoscience,
University of Nebraska, Lincoln, Nebraska 68588-0299, USA

² College of Science, Beijing University of Chemical Technology, Beijing 100029, People's Republic of China

³ Beijing Computational Science Research Center, Beijing 100193, People's Republic of China

The recent discovery of the anomalous Hall effect (AHE) in antiferromagnetic (AFM) materials has stimulated the intense exploration of this phenomenon which may be useful for the emerging field of AFM spintronics. In all these AHE antiferromagnets, however, the net magnetization is allowed by the magnetic space group symmetry, which may limit their use in AFM spintronics. In this letter, we predict a *nonlinear* AHE in the antiferromagnets with symmetry enforced zero net magnetization, thus lifting this limitation. We demonstrate that the presence of a polar axis combined with $\hat{T}\hat{t}_{1/2}$ symmetry in collinear AFM materials leads to a finite Berry curvature dipole and thus a non-zero nonlinear AHE. As a specific example, we consider half Heusler alloy CuMnSb, an AFM Weyl metal, and predict that it exhibits a sizable nonlinear AHE. Based on first-principles density functional theory calculations, we show that multiple Weyl fermions and a large Berry curvature dipole produce a measurable Hall voltage under conventional experimental conditions. The strong dependence of the Berry curvature dipole on the Néel vector orientation provides a new detection scheme of the AFM order based on the nonlinear AHE. Our predictions enrich the material platforms for studying non-trivial phenomena associated with the Berry curvature and broaden the range of materials useful for AFM spintronics.

Over decades, unconventional Hall effects have been a vibrant topic for research in condensed matter physics [1-5]. Among them is the anomalous Hall effect (AHE), which was discovered more than a century ago [6], but remained enigmatic until recently. This is due to the AHE involving, at its core, concepts based on topology that were formulated only in recent years [2]. It is now well understood that there is an intrinsic contribution to the AHE driven by the Berry curvature Ω , a quantity inherent in the electronic band structure of a material [7]. Crystal group symmetry and spin-orbit coupling affect the Berry curvature, and thus control the AHE. For example, Ω is odd under time reversal symmetry \hat{T} , i.e. $\hat{T}\Omega(\mathbf{k}) = -\Omega(-\mathbf{k})$, where \mathbf{k} is the wave vector. Therefore, breaking \hat{T} is necessary to make the integral of Ω over the full Brillouin zone non-vanishing and produce a finite AHE. Due to this property, the AHE is usually found in ferromagnetic materials, where non-zero magnetization breaks \hat{T} symmetry.

Recently, antiferromagnetic (AFM) compounds have attracted growing interest as promising materials for spintronics [8], due to their advantages of being robust against magnetic perturbations, producing zero stray fields, and exhibiting ultrafast magnetization dynamics [9-11]. AFM spintronics exploits the AFM Néel vector to control spin-dependent transport properties. For example, antiferromagnets supporting $\hat{P}\hat{T}$ symmetry (where \hat{P} is space inversion), such as CuMnAs [12], Mn₂Au [13], and MnPd₂ [14], allow the electrical control of the Néel vector by spin-orbit torque. Detecting the anomalous Hall voltage could be a feasible approach to read out the state of the Néel vector in AFM spintronics devices. However, the Berry curvature in these materials is zero due to $\hat{P}\hat{T}\Omega(\mathbf{k}) = -\Omega(\mathbf{k})$, resulting in a vanishing AHE.

Recently, the AHE has been discovered in non-collinear antiferromagnets (Fig. 1(a)), such as Mn₃X (X = Ga, Ge, or Ir) [15-19] and Mn₃AN (A = Ga, Zn, Ag, or Ni) [20-22], and collinear antiferromagnets with specific arrangement of non-magnetic atoms in the crystal lattice (Fig. 1(b)), such as CoNb₃S₆ [23-25]. In all these AFM materials, the non-vanishing AHE is due to the absence of combined symmetry $\hat{T}\hat{O}$ (\hat{O} is a crystal space group symmetry operation), with respect to which the Berry curvature is antisymmetric, i.e. $\hat{T}\hat{O}\Omega(\mathbf{k}') = -\Omega(\mathbf{k})$. This property implies, however, that the net magnetization \mathbf{M} is not forbidden in these antiferromagnets, since no magnetic group symmetry operation $\hat{T}\hat{O}$ would enforce it to be zero, as follows from $\hat{T}\hat{O}\mathbf{M} = -\mathbf{M}$ [26]. As a result, a small net magnetic moment is observed in these materials, which behave like weak ferromagnets [17,18,21,23].

The net magnetization (though small) can be affected by perturbations, influencing the AHE. For example, the net magnetic moment of non-collinear antiferromagnet Mn₃Ge can be switched by a small magnetic field, leading to reversal of the anomalous Hall conductivity [18]. To avoid such instabilities, antiferromagnets with strictly zero net magnetization are desirable for robust AHE-based AFM spintronic devices. Zero magnetization requires, however, the presence of $\hat{T}\hat{O}$ symmetry, which does not support the AHE. Thus, it is impossible to have a *linear* AHE in an antiferromagnet with strictly zero net magnetization.

This problem can be solved with a recently discovered *nonlinear* AHE [27-32]. In contrast to the linear AHE, where the Hall voltage is linear to an applied electric field as found in numerous magnetic (i.e. \hat{T} broken) systems, the nonlinear AHE occurs in second-order response to an electric field as

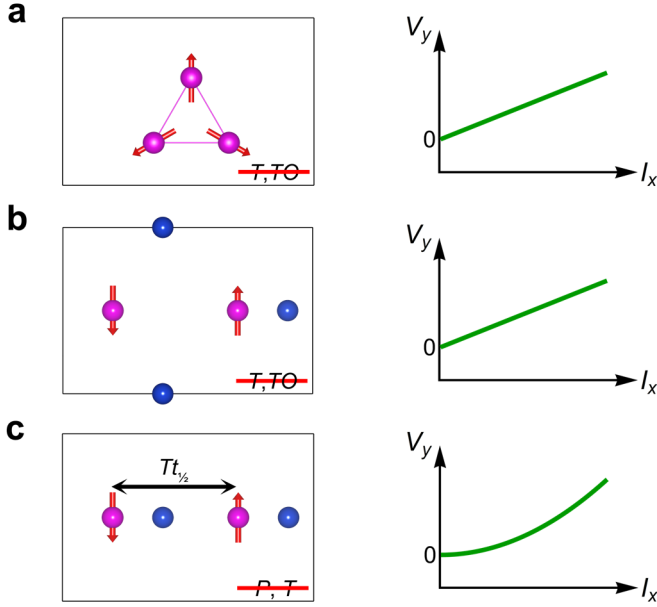


FIG. 1. (a) A non-collinear antiferromagnet with broken \hat{T} and absent $\hat{T}\hat{O}$ symmetry (\hat{O} is a crystal space group symmetry operation), such that $\hat{T}\hat{O}\Omega(\mathbf{k}') = -\Omega(\mathbf{k})$ (left), resulting in a linear AHE (right). (b) A collinear antiferromagnet with a specific arrangement of non-magnetic atoms in the crystal lattice, in which both \hat{T} and $\hat{T}\hat{O}$ symmetries are absent (left), resulting in a linear AHE (right). (c) A collinear antiferromagnet with broken \hat{P} and \hat{T} symmetries but preserved $\hat{T}\hat{t}_{1/2}$ symmetry (left), resulting in a non-linear AHE (right).

demonstrated for a certain class of non-magnetic (i.e. \hat{T} invariant) materials. The nonlinear AHE requires broken \hat{P} symmetry and arises from the Berry curvature dipole \mathbf{D} , which generates a net anomalous velocity when the system is in a current-carrying state [27]. So far, however, the nonlinear AHE has been considered only for non-magnetic materials where \hat{T} symmetry is preserved. Extending this concept to AFM materials where \hat{T} symmetry is broken is interesting and desirable, as it would broaden a range of measurable properties useful for AFM spintronics.

In this letter, we predict that the nonlinear AHE does exist in collinear antiferromagnets with a polar axis and a combined $\hat{T}\hat{t}_{1/2}$ symmetry (where $\hat{t}_{1/2}$ is translation by half a unit cell). As a specific example, we consider half Heusler alloy CuMnSb and demonstrate, based on first-principles density functional theory (DFT) calculations [33], that this collinear antiferromagnet exhibits a sizable nonlinear AHE due to a finite Berry curvature dipole. Moreover, we find that CuMnSb supports multiple Weyl fermions around the Fermi energy, which contribute to the nonlinear AHE in a non-trivial way. Finally, we predict a strong dependence of the Berry curvature dipole and hence the nonlinear AHE on the AFM Néel vector orientation, the property which does not exist in non-magnetic materials but may be useful for applications.

The Berry curvature dipole density tensor \mathbf{d} is defined as $d_{bd} = -\frac{\partial f_0}{\partial k_b} \Omega^d$, where k_b and Ω^d are Cartesian components of the wave vector and the Berry curvature, respectively, and f_0 is the equilibrium Fermi distribution function. It is odd under space inversion, and therefore the nonlinear AHE in antiferromagnets requires a non-centrosymmetric structure. In fact, the condition is even more stringent and, similar to non-magnetic systems, necessitates the presence of certain symmetry constraints [27]. Here, we consider collinear antiferromagnets with a polar axis and $\hat{T}\hat{t}_{1/2}$ symmetry (Fig. 1(c)). These conditions are sufficient for the nonlinear AHE to emerge, due to \mathbf{d} being even under the $\hat{T}\hat{t}_{1/2}$ transformation, i.e. $\hat{T}\hat{t}_{1/2}\mathbf{d}(\mathbf{k}) = \mathbf{d}(-\mathbf{k})$.

Among the AFM materials with the required symmetry properties, we identify half Heusler alloy CuMnSb. Figs. 2(a,b) show the crystal structure of CuMnSb that belongs to the crystal space group $F\bar{4}3m$ [34,35]. Below the Néel temperature $T_N = 55$ K, a type-II collinear AFM order emerges, where the magnetic moments of the Mn atoms are parallel within the (111) plane but antiparallel between the successive (111) planes (Fig. 2(a)). The Néel vector is pointed along the [111] direction, leading to magnetic space group $R\bar{3}c$ [35]. The rhombohedral primitive cell of CuMnSb (Fig. 2(b)) contains three-fold rotation \hat{C}_3 around the [111] direction, and three glide mirror reflections $\hat{g}_{\bar{1}10}$, $\hat{g}_{\bar{1}01}$, and $\hat{g}_{0\bar{1}1}$, where $\hat{g}_l = \{\hat{M}_l | \hat{t}_{1/2}\}$ is mirror symmetry \hat{M}_l normal to vector \mathbf{l} combined with half a unit cell translation $\hat{t}_{1/2}$. In addition, below 34 K the Néel vector is canted towards the [110] direction by $\delta = 11^\circ$ [35,36]. This canting breaks the \hat{C}_3 , $\hat{g}_{\bar{1}01}$, and $\hat{g}_{0\bar{1}1}$ symmetries, leading to the magnetic space group C_{2v} in which only $\hat{g}_{\bar{1}10}$ is preserved [35]. Both AFM phases of CuMnSb are polar and contain the $\hat{T}\hat{t}_{1/2}$ symmetry.

First, we investigate the AFM phase of CuMnSb without canting. Assuming the experimental lattice constant $a = 6.075$ Å, we find the calculated magnetic moment of $3.93 \mu_B/\text{Mn}$ consistent with the experimental value of $3.9 (\pm 0.1) \mu_B/\text{Mn}$ [35]. Fig. 2(c) shows the calculated band structure. There are six bands crossing the Fermi energy E_F , mostly contributed by $3d$ electrons of Mn [37] (Fig. S1). The four valence bands are very dispersive with the maximum around the Γ point, forming four hole pockets along the Γ -Z direction. The conduction band minimum is less dispersive, forming electron pockets near the edges of the top and bottom surfaces of the Brillouin zone (Fig. S1). There are multiple crossings or anticrossings in the band structure near E_F . For example, in Figs. 2(c,d) we show the band crossings by the second and third valence bands (purple lines). As seen from Fig. 2(d), there are two Weyl points at $E = 0.102$ eV (W_1) and $E = -0.051$ eV (W_2). The band crossings close to the Weyl points are strongly tilted. As is evident from in Fig. 2(e), W_1 and W_2 are located at the touching points of the two Fermi pockets. This indicates that W_1 and W_2 are type-II Weyl

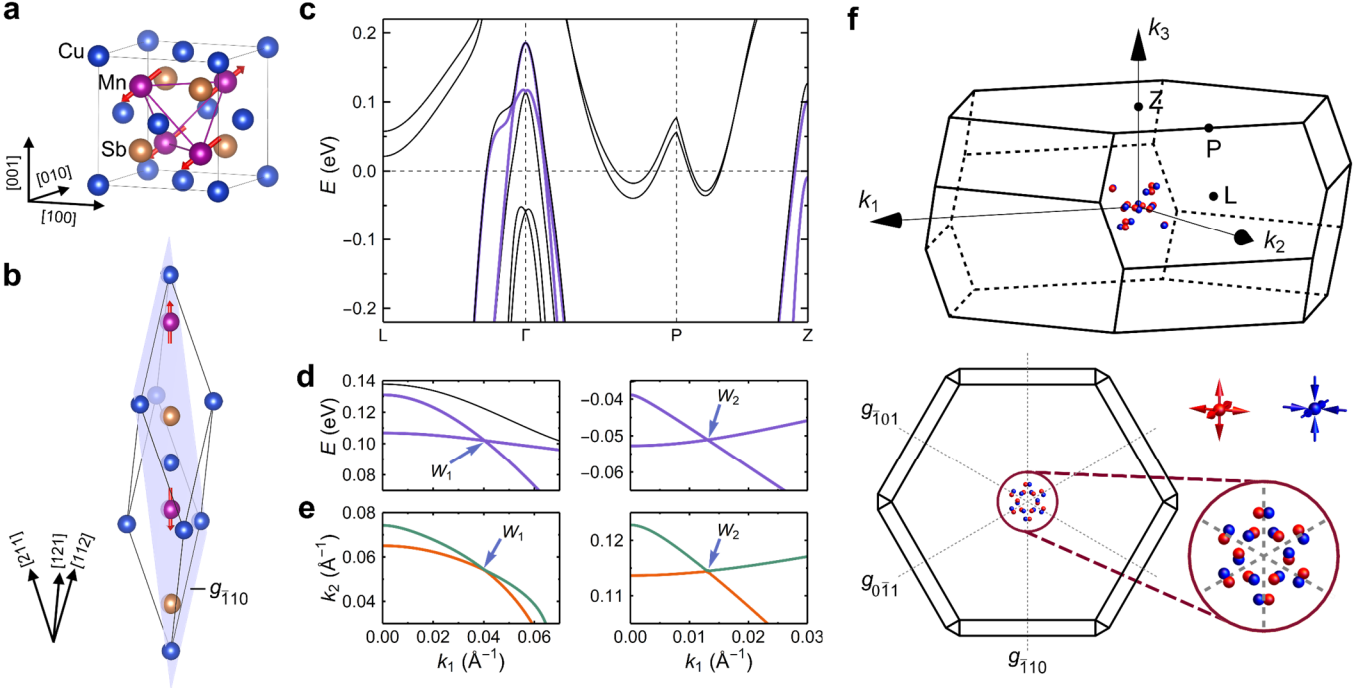


FIG. 2. (a,b) The collinear AFM magnetic structure of CuMnSb shown in a conventional cubic unit cell (a) and a rhombohedral primitive cell (b). Red arrows denote the magnetic moments of Mn. The light blue plane denotes the glide plane \hat{g}_{110} . (c) The band structure of CuMnSb near E_F . (d) The band structures close to Weyl points W_1 with $k_2 = 0.054 \text{ \AA}^{-1}$ and $k_3 = 0.004 \text{ \AA}^{-1}$ (left) and W_2 with $k_2 = 0.115 \text{ \AA}^{-1}$ and $k_3 = 0.081 \text{ \AA}^{-1}$ (right). Here k_1 , k_2 , and k_3 are along the $[\bar{1}10]$, $[\bar{1}\bar{1}2]$, and $[111]$ directions in the cubic lattice. The purple lines in (c,d) denote the two bands forming Weyl points. The horizontal dashed line indicates the Fermi energy. (e) The Fermi surfaces at $k_3 = 0.004 \text{ \AA}^{-1}$ and $E = 0.102 \text{ eV}$ (left) and at $k_3 = 0.081 \text{ \AA}^{-1}$ and $E = -0.051 \text{ eV}$ (right). The Weyl points locate at the intersection points of the Fermi surfaces. (f) The side view and the top view of the Weyl points in the Brillouin zone. The red and blue colors denote the monopole charges $+1$ and -1 of the Weyl points, respectively.

fermions [38, 39]. By application of $\hat{T}\hat{\tau}_{1/2}$, \hat{C}_3 , and glide symmetry transformations to W_1 and W_2 , we obtain six pairs of W_1 and six pairs of W_2 Weyl fermions located in the central part of the Brillouin zone (Fig. 2(f)).

Next, we discuss the nonlinear Hall response. Electric field $\mathbf{E}_c = \text{Re}\{\mathcal{E}e^{i\omega t}\}$ of amplitude \mathcal{E} and frequency ω produces nonlinear current $J_a = \text{Re}\{J_a^{(0)} + J_a^{(2)}e^{i2\omega t}\}$, where $J_a^{(0)} = \chi_{abc}^{(0)}\mathcal{E}_b\mathcal{E}_c^*$ and $J_a^{(2)} = \chi_{abc}^{(2)}\mathcal{E}_b\mathcal{E}_c^*$. For a system with time reversal symmetry, the response coefficients are [27]:

$$\chi_{abc}^{(0)} = \chi_{abc}^{(2)} = -\epsilon_{adc} \frac{e^3 \tau D_{bd}}{2\hbar^2(1 + i\omega\tau)}, \quad (1)$$

where τ is the relaxation time, and D_{bd} is the Berry curvature dipole defined as

$$D_{bd} = \int \frac{d^3k}{(2\pi)^3} d_{bd} = - \int \frac{d^3k}{(2\pi)^3} \sum_n \frac{\partial E_{nk}}{\partial k_b} \Omega_{nk}^d \frac{\partial f_0}{\partial E_{nk}}. \quad (2)$$

Here E_{nk} is the energy of the n -th band at the \mathbf{k} point. The Berry curvature of the n -th band is given by [7]:

$$\Omega_{nk}^d = i\epsilon_{abd} \sum_{m \neq n} \frac{\langle n | \frac{\partial H}{\partial k_a} | m \rangle \langle m | \frac{\partial H}{\partial k_b} | n \rangle}{(E_{nk} - E_{mk})^2}. \quad (3)$$

The factor $\frac{\partial E_{nk}}{\partial k_b}$ is odd under both \hat{P} and \hat{T} symmetries and Ω_{nk}^d is odd under \hat{T} and even under \hat{P} . As a result, d_{bd} in Eq. (2) is even with respect to \hat{T} , leading to non-zero D_{bd} and a finite nonlinear AHE in a non-centrosymmetric system without magnetism. In an antiferromagnet like CuMnSb, the preserved $\hat{T}\hat{\tau}_{1/2}$ symmetry plays the same role as \hat{T} on $\frac{\partial E_{nk}}{\partial k_b}$ and Ω_{nk}^d , and the polar axis ensures a nonzero \mathbf{D} . Therefore, a finite D_{bd} can be also expected in such a collinear antiferromagnet.

There is only one independent element of the \mathbf{D} tensor in the AFM phase without canting (Table SII) [33]. For definiteness, we consider D_{xz} directly related to $J_y = \chi_{yxx}\mathcal{E}_x^2$, a transverse nonlinear Hall current along the y ($[010]$) direction produced by a longitudinal electric field along the x ($[100]$) direction. Figs. 3(a,b) show the projection of D_{xz} on the k_1 - k_2 plane, at $E = 0.102 \text{ eV}$ (Fig. 3(a)) and $E = -0.051 \text{ eV}$ (Fig. 3(b)), which is obtained by integration $\int \frac{dk_3}{2\pi} d_{xz}$. According to Eq. (2), D_{xz} is a Fermi-surface property, and thus only the Fermi pockets contribute to D_{xz} . We find that the contribution by the Fermi pockets from the conduction bands is negligible compared to those from the valence bands. This is due to the valence bands near their maximum having stronger dispersion,

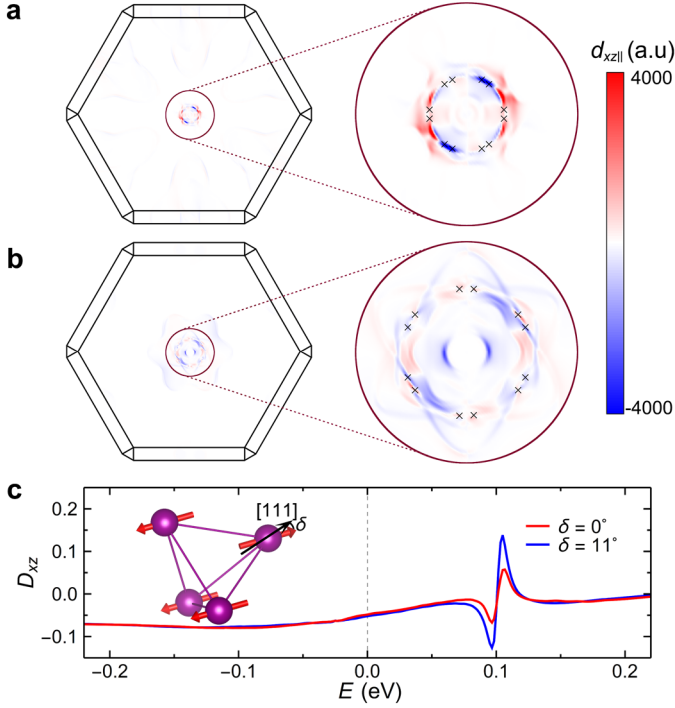


FIG. 3. (a,b) The projections of the Berry curvature dipole on k_1 - k_2 plane at $E = 0.102$ eV (a) and $E = -0.051$ eV (b). Black cross symbols denote position of the Weyl fermions. (c) The D_{xz} as a function of energy for the AFM phase without (red line) and with (blue line) canting of the Néel vector. The inset schematically shows the canting.

which leads to larger velocity $v_x = \frac{\partial E_{nk}}{\partial k_x}$ (Fig. 2(c)). On the other hand, the gaps between the valence bands are very small near E_F , which leads to larger Ω_{nk}^z according to Eq. (3). Therefore, as seen from the energy dependence of D_{xz} in Fig. 3(c), the magnitude of D_{xz} increases with energy decreasing, due to the increase of the volume of the central Fermi surfaces from the valence bands. The calculated D_{xz} is about -0.048 at E_F , and can be enhanced to -0.080 by proper doping (Fig. 3(c)). These values are comparable to those obtained for non-magnetic metals [29,30], and can lead to a sizeable non-linear Hall voltage with a conventional experimental set-up [33].

We note that the contributions of the Weyl fermions W_1 and W_2 to D_{xz} are different. The states near W_1 dominate D_{xz} around $E = 0.102$ eV, as shown in Figs. 3(a) and S4, leading to the anomaly in the D_{xz} curve at this energy (Fig. 3(c)). On the other hand, there is no pronounced contributions from W_2 (Fig. 3(b)) due to very small v_x near W_2 , which suppresses the anomaly in the D_{xz} curve at $E = -0.051$ eV (Fig. 3(c)).

At low temperature, the Néel vector is tilted towards the $[110]$ direction by $\delta = 11^\circ$ [35]. This weak canting leads to tiny changes of the band structure (Fig. S2). Nevertheless, breaking the \hat{C}_3 , \hat{g}_{101} , and $\hat{g}_{0\bar{1}1}$ symmetries alters the number and the positions of the Weyl fermions (Fig. S2). The energy dependence of D_{xz} in this AFM phase is generally similar to

that in the AFM phase without canting, except sharper peaks above E_F due to the different distribution of the Weyl points (Figs. 3(c) and S2). Moreover, the change of symmetry influences the \mathbf{D} tensor [33], resulting in different magnitudes of D_{xy} and D_{xz} (Table SII). This difference can be further enhanced by stronger canting. For example, for the canting angle of $\delta = 90^\circ$ (similar to that in a half Heusler alloy GdMnBi [40]), we find $D_{xy} = 0.072$ being much larger than D_{xz} (Table SII). Since D_{xy} is related to the Hall current J_z , the large difference between D_{xy} and D_{xz} will lead to different nonlinear Hall responses in y and z directions, which can be used to detect Néel vector canting.

The sensitivity of the Berry curvature dipole to the Néel vector implies tunability of the nonlinear AHE in CuMnSb. Doping [41] and ferroelastic strain [42] can be used to control Néel vector canting. Moreover, the type-II AFM order with the Néel vector normal to the (111) planes is energetically identical to that normal to the $(\bar{1}\bar{1}1)$, $(1\bar{1}\bar{1})$, or $(11\bar{1})$ planes. Switching between these orders is expected to reverse the Hall voltage. For example, switching the Néel vector from (111) to $(\bar{1}\bar{1}1)$ is equivalent to C_3 rotation around the $[11\bar{1}]$ direction. This operation swaps D_{xz} for $-D_{yx}$. In an AFM phase without canting, this leads to a sign change of V_y . If the canting is tuned to $\delta = 90^\circ$, in addition to the sign reversal, such a switching changes the magnitude of V_y by 77%.

The predicted effect is not limited to CuMnSb but expected to exist in other AFM metals with the appropriate symmetry, such as PdMnTe [43] and $\text{Ca}_3\text{Ru}_2\text{O}_7$ [44]. All these materials have globally non-centrosymmetric structures, and therefore an electric current is expected to generate an antidamping-like spin-orbit torque, alternating in sign between the two AFM sublattices [12, 45,46]. If the current is sufficiently strong, this staggered spin-orbit torque can be used to switch the Néel vector, which can be detected by measuring the non-linear AHE.

In conclusion, we have predicted that collinear AFM metals with a polar axis and $\hat{T}\hat{t}_{1/2}$ symmetry exhibit a nonlinear AHE. As an example, we considered half Heusler alloy CuMnSb and showed that this antiferromagnet has a large Berry curvature dipole resulting in a sizable nonlinear AHE. Furthermore, we found that CuMnSb supports multiple Weyl fermions around the Fermi energy, producing an anomaly in the nonlinear AHE as a function of energy. The strong dependence of the Berry curvature dipole on the Néel vector orientation provides a new detection scheme of the AFM order based on the non-linear AHE, which may be useful for AFM spintronics. We hope therefore that our theoretical predictions will motivate experimentalists to explore the nonlinear AHE in antiferromagnets.

Acknowledgments. The authors thank Ruichun Xiao and Bo Li for helpful discussions. This work was supported by the National Science Foundation (NSF) through the Nebraska

MRSEC program (grant DMR-1420645) and the DMREF program (grant DMR-1629270). S.-H.Z thanks the support of National Science Foundation of China (NSFC Grants No. 11504018 and No. 11774021). Computations were performed at the University of Nebraska Holland Computing Center.

* These authors contributed equally to this work.

† dfshao@unl.edu

‡ shuizhang@mail.buct.edu.cn

§ tsymbal@unl.edu

- [1] B. Keimer and J. E. Moore, The physics of quantum materials, *Nat. Phys.* **13**, 1045 (2017).
- [2] N. Nagaosa, J. Sinova, S. Onoda, A. H. MacDonald, and N. P. Ong, Anomalous Hall effect, *Rev. Mod. Phys.* **82**, 1539 (2010).
- [3] J. Sinova, S. O. Valenzuela, J. Wunderlich, C. H. Back, and T. Jungwirth, Spin Hall effects, *Rev. Mod. Phys.* **87**, 1213 (2015).
- [4] Klaus von Klitzing, The quantized Hall effect, *Rev. Mod. Phys.* **58**, 519 (1986).
- [5] J. Wang and S.-C. Zhang, Topological states of condensed matter, *Nat. Mater.* **16**, 1062 (2017).
- [6] E. Hall, *Philos. Mag.* **12**, 157 (1881).
- [7] D. Xiao, M.-C. Chang, and Q. Niu, Berry phase effects on electronic properties, *Rev. Mod. Phys.* **82**, 1959 (2010).
- [8] E. Y. Tsymbal and I. Žutić Eds., *Spintronics Handbook: Spin Transport and Magnetism*, 2nd edition (CRC press, 2019).
- [9] V. Baltz, A. Manchon, M. Tsoi, T. Moriyama, T. Ono, and Y. Tserkovnyak, Antiferromagnetic spintronics, *Rev. Mod. Phys.* **90**, 015005 (2018).
- [10] T. Jungwirth, X. Marti, P. Wadley, and J. Wunderlich, Antiferromagnetic spintronics, *Nat. Nanotech.* **11**, 231 (2016).
- [11] L. Šmejkal, Y. Mokrousov, B. Yan, and A. H. MacDonald, Topological antiferromagnetic spintronics, *Nat. Phys.* **14**, 242 (2018).
- [12] P. Wadley, B. Howells, J. Železný, C. Andrews, V. Hills, R. P. Campion, V. Novák, K. Olejník, F. Maccherozzi, S. S. Dhesi, S. Y. Martin, T. Wagner, J. Wunderlich, F. Freimuth, Y. Mokrousov, J. Kuneš, J. S. Chauhan, M. J. Grzybowski, A. W. Rushforth, K. W. Edmonds, B. L. Gallagher, and T. Jungwirth, Electrical switching of an antiferromagnet, *Science* **351**, 587(2016).
- [13] S. Y. Bodnar, L. Šmejkal, I. Turek, T. Jungwirth, O. Gomonay, J. Sinova, A. A. Sapozhnik, H.-J. Elmers, M. Kläui, and M. Jourdan, Writing and reading antiferromagnetic Mn₂Au by Néel spin-orbit torques and large anisotropic magnetoresistance, *Nat. Commun.* **9**, 348 (2018).
- [14] D.-F. Shao, G. Gurung, S.-H. Zhang, and E. Y. Tsymbal, Dirac nodal line metal for topological antiferromagnetic spintronics, *Phys. Rev. Lett.* **122**, 077203 (2019).
- [15] H. Chen, Q. Niu, and A. H. MacDonald, Anomalous Hall effect arising from noncollinear antiferromagnetism, *Phys. Rev. Lett.* **112**, 017205 (2014).
- [16] J. Kübler and C. Felser, Non-collinear antiferromagnets and the anomalous Hall effect, *EPL* **108**, 67001 (2014).
- [17] S. Nakatsuji, N. Kiyohara, and T. Higo, Large anomalous Hall effect in a non-collinear antiferromagnet at room temperature, *Nature* **527**, 212 (2015).
- [18] A. K. Nayak, J. E. Fischer, Y. Sun, B. Yan, J. Karel, A. C. Komarek, C. Shekhar, N. Kumar, W. Schnelle, J. Kübler, C. Felser, and S. P. P. Parkin, Large anomalous Hall effect driven by a nonvanishing Berry curvature in the noncollinear antiferromagnet Mn₃Ge, *Sci. Adv.* **2**, e1501870 (2016).
- [19] Y. Zhang, Y. Sun, H. Yang, J. Železný, S. P. P. Parkin, C. Felser, and B. Yan, Strong anisotropic anomalous Hall effect and spin Hall effect in the chiral antiferromagnetic compounds Mn₃X (X=Ge, Sn, Ga, Ir, Rh, and Pt), *Phys. Rev. B* **95**, 075128 (2017).
- [20] G. Gurung, D.-F. Shao, T. R. Paudel, and E. Y. Tsymbal, Anomalous Hall conductivity of non-collinear magnetic antiperovskites, *Phys. Rev. Mater.* **3**, 044409 (2019).
- [21] D. Boldrin, I. Samathrakakis, J. Zemen, A. Mihai, B. Zou, B. Esser, D. McComb, P. Petrov, H. Zhang, and L. F. Cohen, The anomalous Hall effect in non-collinear antiferromagnetic Mn₃NiN thin films, arXiv:1902.04357 (2019).
- [22] X. Zhou, J. -P. Hanke, W. Feng, F. Li, G.-Y. Guo, Y. Yao, S. Blügel, and Y. Mokrousov, Spin-order dependent anomalous Hall effect and magneto-optical effect in the noncollinear antiferromagnets Mn₃XN with X = Ga, Zn, Ag, or Ni, *Phys. Rev. B* **99**, 104428 (2019).
- [23] N. J. Ghimire, A. S. Botana, J. S. Jiang, J. Zhang, Y.-S. Chen, and J. F. Mitchell, Large anomalous Hall effect in the chiral-lattice antiferromagnet CoNb₂S₆, *Nat. Commun.* **9**, 3280 (2018).
- [24] L. Šmejkal, R. González-Hernández, T. Jungwirth, and J. Sinova, Crystal Hall effect in collinear antiferromagnets, arXiv:1901.00445 (2019).
- [25] X. Li, A. H. MacDonald, and H. Chen, Quantum anomalous Hall effect through canted antiferromagnetism, arXiv:1902.10650 (2019).
- [26] H. Chen, T. -C. Wang, D. Xiao, G. -Y. Guo, Q. Niu, and A. H. MacDonald, Manipulating anomalous Hall antiferromagnets with magnetic fields, arXiv:1802.03044 (2018).
- [27] I. Sodemann and L. Fu, Quantum nonlinear Hall effect induced by Berry curvature dipole in time-reversal invariant materials, *Phys. Rev. Lett.* **115**, 216806 (2015).
- [28] Z. Z. Du, C. M. Wang, H. -Z. Lu, and X. C. Xie, Band signatures for strong nonlinear Hall effect in bilayer WTe₂, *Phys. Rev. Lett.* **121**, 266601 (2018).
- [29] Y. Zhang, Y. Sun, and B. Yan, Berry curvature dipole in Weyl semimetal materials: An *ab initio* study, *Phys. Rev. B* **97**, 041101(R) (2018).
- [30] J. I. Facio, D. Efremov, K. Koepf, J. -S. You, I. Sodemann, and J. van den Brink, Strongly enhanced Berry dipole at topological phase transitions in BiTeI, *Phys. Rev. Lett.* **121**, 246403 (2018).
- [31] Q. Ma, S. -Y. Xu, H. Shen, D. MacNeill, V. Fatemi, T. -R. Chang, A. M. Mier Valdivia, S. Wu, Z. Du, C. -H. Hsu, S. Fang, Q. D. Gibson, K. Watanabe, T. Taniguchi, R. J. Cava, E. Kaxiras, H. -Z. Lu, H. Lin, L. Fu, N. Gedik, and Pa. Jarillo-Herrero, Observation of the nonlinear Hall effect under time-reversal-symmetric conditions, *Nature* **565**, 337-342 (2019).
- [32] K. Kang, T. Li, E. Sohn, J. Shan, and K. F. Mak, Nonlinear anomalous Hall effect in few-layer WTe₂, *Nat. Mater.* **18**, 324 (2019).
- [33] See Supplemental Material.
- [34] K. Endo, T. Ohoyama, and R. Kimura, Antiferromagnetism of CuMnSb, *J. Phys. Soc. Jpn.* **25**, 907 (1968).
- [35] A. Regnat, A. Bauer, A. Senyshyn, M. Meven, K. Hradil, P. Jorba, K. Nemkovski, B. Pedersen, R. Georgii, S. Gottlieb-Schönmeier, and C. Pfleiderer, Canted antiferromagnetism in phase-pure CuMnSb, *Phys. Rev. Mater.* **2**, 054413 (2018).

- [36] F. Máca, J. Kudrnovský, V. Drchal, I. Turek, O. Stelmakhovich, P. Beran, A. Llobet, and X. Marti, Defect-induced magnetic structure of CuMnSb, *Phys. Rev. B* **94**, 094407 (2016).
- [37] T. Jeong, Ruben Weht, and W. E. Pickett, Semimetallic antiferromagnetism in the half-Heusler compound CuMnSb, *Phys. Rev. B* **71**, 184103 (2005).
- [38] N. P. Armitage, E. J. Mele, and A. Vishwanath, Weyl and Dirac semimetals in three-dimensional solids, *Rev. Mod. Phys.* **90**, 015001 (2018).
- [39] A. A. Soluyanov, D. Gresch, Z. Wang, Q. S. Wu, M. Troyer, X. Dai, and B. A. Bernevig, Type-II Weyl semimetals, *Nature* **527**, 495-498 (2016).
- [40] R. A. Müller, N. R. Lee-Hone, L. Lapointe, D. H. Ryan, T. Pereg-Barnea, A. D. Bianchi, Y. Mozharivskyj, and R. Flacau, Magnetic structure of GdBiPt: A candidate antiferromagnetic topological insulator, *Phys. Rev. B* **90**, 041109(R) (2014).
- [41] I. A. Zhuravlev, A. Adhikari, and K. D. Belashchenko, Perpendicular magnetic anisotropy in bulk and thin-film CuMnAs for antiferromagnetic memory applications, *Appl. Phys. Lett.* **113**, 162404 (2018).
- [42] X. Chen, X. Zhou, R. Cheng, C. Song, J. Zhang, Y. Wu, Y. Ba, H. Li, Y. Sun, Y. You, Y. Zhao, and F. Pan, Electric field control of Néel spin-orbit torque in an antiferromagnet, *Nature Mater.* doi: 10.1038/s41563-019-0424-2 (2019).
- [43] R. B. Helmholtz and K. H. J. Buschow, A neutron diffraction and magnetization study of PdMnTe, *J. LessCommon Met.* **123**, 169 (1986).
- [44] Y. Yoshida, S.-I. Ikeda, H. Matsuhata, N. Shirakawa, C. H. Lee, and S. Katano, Crystal and magnetic structure of Ca₃Ru₂O₇, *Phys. Rev. B* **72**, 054412 (2005).
- [45] J. Železný, H. Gao, A. Manchon, F. Freimuth, Y. Mokrousov, J. Zemen, J. Mašek, J. Sinova, and T. Jungwirth, Spin-orbit torques in locally and globally noncentrosymmetric crystals: Antiferromagnets and ferromagnets, *Phys. Rev. B* **95**, 014403 (2017).
- [46] A. Manchon, J. Zelezný, I. M. Miron, T. Jungwirth, J. Sinova, A. Thiaville, K. Garello, and P. Gambardella, Current-induced spin-orbit torques in ferromagnetic and antiferromagnetic systems, arXiv:1801.09636 (2018).